Journal Pre-proofs

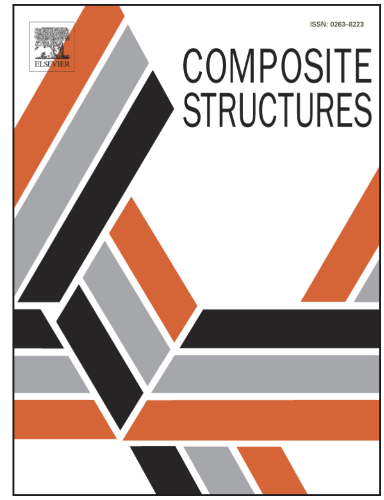

Modelling Hollow Pultruded FRP Profiles under Axial Compression: Local Buckling and Progressive Failure

Mohammad Alhawamdeh, Omar Alajarmeh, Thiru Aravinthan, Tristan Shelley, Peter Schubel, Michael Kemp, Xuesen Zeng

PII: S0263-8223(21)00111-2
DOI: https://doi.org/10.1016/j.compstruct.2021.113650
Reference: COST 113650

To appear in: *Composite Structures*

Received Date: 6 September 2020
Revised Date: 26 December 2020
Accepted Date: 26 January 2021

Please cite this article as: Alhawamdeh, M., Alajarmeh, O., Aravinthan, T., Shelley, T., Schubel, P., Kemp, M., Zeng, X., Modelling Hollow Pultruded FRP Profiles under Axial Compression: Local Buckling and Progressive Failure, *Composite Structures* (2021), doi: https://doi.org/10.1016/j.compstruct.2021.113650

Modelling Hollow Pultruded FRP Profiles under Axial Compression: Local Buckling and Progressive Failure

Mohammad Alhawamdeh[1], Omar Alajarmeh[1], Thiru Aravinthan[1], Tristan Shelley[1], Peter Schubel[1], Michael Kemp[2], Xuesen Zeng*[1]

*Corresponding author: xuesen.zeng@usq.edu.au, University of Southern Queensland West Street Toowoomba Qld 4350 Australia

[1] University of Southern Queensland, Centre for Future Materials, Toowoomba Queensland Australia 4350

[2] Wagners Composite Fibre Technologies, Wellcamp Queensland Australia 4350

ABSTRACT

Pultruded Fibre-Reinforced Polymer (PFRP) profiles are widely used as structural elements in many civil infrastructure applications. However, the anisotropic elasticity and the application-driven slenderness make these profiles prone to local buckling failure, well below their ultimate load capacity. In this paper, a numerical study was undertaken to characterise the local buckling and compressive failure of hollow PFRP profiles under axial compression. The Newton method were used along with the adaptive automatic stabilisation scheme and a controlled increment size in Abaqus 2019, to overcome the numerical difficulties in simulating local buckling. The numerical predictions were validated by experiments. The energy parameters and the constituent failure modes of the FEM models were used to explain the effect of dimension, layup, and slenderness ratio on the post-peak behaviour and failure modes of the PFRP profiles. Moreover, the reliance of the strain energy restoration after buckling and the axial and transverse deformations on these parameters was explained.

Keywords: Hollow GFRP columns, compressive failure, finite element modelling, local buckling, progressive failure.

1. INTRODUCTION

Pultruded Fibre-Reinforced Polymer (PFRP) profiles flourished through the previous few decades. They became reliable structural construction elements as beams and trusses in buildings and bridges [1,2], piles in deep foundations [3], frames in marine structures [4,5], lighting poles and cross-arms in electrical infrastructure [6,7], pipes in the oil industry, spar caps for wind turbines and cable trays and grating walkways in solar structures in the energy sector [8–10], reinforcements for concrete [11], and sleepers in railways [12,13]

The anisotropic properties of laminated composites provide a broader design range than other materials. However, it presents compressive design difficulties inherited from the high slenderness, which can result in local instabilities such as local buckling [1,6,14–19]. Local buckling is one of the major failure modes dictating the hollow box PFRP profile behaviour. Experimentally, it can occur before the structural elements reach their ultimate strength limits [1,5,17,20,21]. On the other hand, hollow circular PFRP profiles are less prone to local buckling and show compressive and shear failure due to the high circumferential confining stresses [22]. Understanding the failure and energy mechanisms accompanying local buckling of composites, experimentally, presents a challenge which requires a sophisticated test setup and measurement techniques to be overcome [2,20].

The numerical approach represented by the Finite Element Method (FEM) is a robust tool to model and analyse the structural behaviour of PFRP profiles and investigate their capability and behaviour under specific loading conditions [23–29]. However, special care should be taken when studying and modelling local buckling behaviour of composites with FEM since there are several numerical methods implemented with each one of them containing advantages and limitations [14,30–32]. These methods are the linear eigenvalue (linear perturbation), the modified Riks/Arc-length, Newton method, and the dynamic analysis. The compressive behaviour of hollow square PFRP profiles has been studied numerically [33–35]. In these studies, the linear static solver STRAND 7 was used to investigate the elastic behaviour and load capacity of stub columns with different length-to-width ratios varying from 1 to 5. The captured failure mode ranged from buckling bulge for a ratio of 1 to local buckling for a ratio of 5. Moreover, the linear perturbation procedure in Abaqus was used to simulate the local buckling of hollow box and channel-section Fibre-Reinforced Polymer (FRP) short columns and beams through an eigenvalue buckling problem [36–42]. However, in all these studies, the full load-displacement path and progressive failure were not simulated due to limitations in the analysis method utilised. Linear eigenvalue buckling was also introduced to determine buckling modes of I-shape and tubular FRP pultruded short columns using Abaqus and ANSYS [43–46]. These modes were implemented as geometric imperfections to a nonlinear modified Riks method/Arc-length method analysis to estimate the buckling, post-buckling, and failure loads. The predicted nonlinear FEM results were higher than the linear FEM results and reasonably agreed with the experimental results. Nevertheless, this approach was limited to study global buckling and its effects. The Newton method was used to simulate the buckling of axially loaded I-shape, C-shape, and box FRP profiles through a nonlinear geometric analysis in ANSYS and Abaqus [47–49]. The FEM results closely matched the experimental results. However, these studies did not focus on local instabilities. In explicit dynamic solvers such as Abaqus/Explicit, dynamic nonlinear geometric analysis can be performed to capture local instabilities. This approach does not suffer from convergence problems due to its central-difference operator, and it allows for progressive failure definition. However, many numerical parameters such as, mass-scaling, artificial damping, and loading-rate present difficulties [31,50].

From the previous studies, the advantages and limitations of each FEM buckling analysis method can be summarised. The linear eigenvalue buckling method has been extensively used in literature to model the buckling of laminated profiles due to its simple eigenvalue algorithm which exists in most FEM packages and its low computational requirement. Nevertheless, it can only provide accurate results for perfect geometries and cannot capture nonlinear geometry, post-buckling, and progressive failure behaviour [19,43,51–53]. Quasi-static (implicit) solvers, such as Abaqus/Standard, provide a nonlinear geometric analysis for global instabilities based on modified Riks/Arc-length method. It is a load-incremental method which has no convergence issues and can capture severe geometric nonlinearities and post-buckling behaviour. Despite that, it faces limitations against local instabilities and needs a geometric imperfection history as it cannot capture the bifurcation point [52,54]. The Newton method on the other hand can model severe geometric nonlinearities and post-buckling along with progressive failure through a nonlinear geometric time-incremental analysis. Yet, some drawbacks can be observed in this method which are related to the localised release of the strain energy (damping issues) and increment size (convergence issues) which form numerical parameters unmeasurable by direct experiments [46].

In this research, the Newton method in Abaqus/Standard will be used along with the adaptive automatic stabilisation scheme and controlled increment size to overcome numerical difficulties in simulating the localised release of the strain energy and the solution convergence, respectively. A simplified three-dimensional modelling approach will be established to perform a nonlinear geometric analysis of local buckling and progressive failure behaviours of PFRP profiles, without the need for special codes and intensive programming. This study will demonstrate an efficient modelling tool to assist the design and optimisation stage of new product development, with aims to reduce high costs associated with extensive experimental testing and post-manufacturing characterisation.

2. EXPERIMENTAL PROGRAM

2.1 Materials and structures

Four hollow PFRP profile geometries were experimentally tested under axial compression to assist in validating the FEM approach presented herein. The PFRP profiles investigated in this research were all manufactured by Wagners CFT and consist of E-glass fibres & Vinyl-Ester polymer resin. The hollow box profiles have corners with an inner and outer radii of 4.75 mm and 10 mm, respectively. The experimental program considered various length-to-width (L/D) ratios for the stub columns (ranging from 2 to 5). Assessing the FEM results for different L/D ratios provides the sensitivity of the proposed modelling to the dimensional changes. The geometric and cross-sectional details of the profiles experimentally tested are provided in Table 1 and Fig. 1, respectively. Moreover, experimental data from a previous study using Wagners CFT products [33] was extracted for validation purposes to complement the profiles tested in the current study (also reported in Table 1 and Fig. 1).

The composite layup of the profiles was provided by Wagners CFT (Table 2). The two hollow circular profiles differ only in their layups; C1-89×6.0 has a higher percentage of axial fibres and 56^{o} inclined fibres, while C2-89×6.0 has a lower percentage of axial fibres and 71^{o} inclined fibres.

2.2 Test setup

The experimental program was conducted under a quasi-static loading rate of 1 mm/min with fixed-fixed supports at the profile ends. Steel fixtures were used to constrain the profile ends to prevent localised premature failure. Fig. 2 illustrates the axial compression testing configuration using a SANS (SHT4206 – 2000 kN capacity) universal testing machine loaded with a specimen. The load-axial displacement data was recorded using a Linear Variable Differential Transducer

(LVDT) unit at the bottom-loading cell. Strain gauges mounted longitudinally and transversely at the specimens' mid-height were used to calculate the axial modulus values.

3. FINITE ELEMENT MODELLING

3.1 Elastic behaviour

The elastic lamina material definition was selected as it is suited for 2D plane stress formulation, such as in laminated shells [50]. The lamina mechanical properties of the PFRP profiles used in this study, along with their respective fibre volume fraction (V_f), are shown in Table 3. The lamina mechanical properties were calculated using the fibre volume fraction, provided by Wagners CFT. The previous studies [33, 34] experimentally characterised the same profiles currently being studied. The fibre volume fraction was obtained from the burnout test, which confirmed the values in the manufacturer datasheets. The theoretical mechanical properties were verified against the coupon-level and structural-level experimental tests. The elastic modulus in the fibre direction (E_1) was calculated using the rule of mixture. Whereas the transverse elastic modulus (E_2), the in-plane shear modulus (G_{12}), and the out-of-plane shear modulus (G_{23}) were calculated using empirical equations [33,34,55]. The value of (G_{13}) was set to equal the value of (G_{12}) since unidirectional plies are considered to be transversely isotropic materials [20].

3.2 Progressive failure behaviour

The Hashin damage model (1980) was used to simulate the progressive failure in fibres and matrix at the lamina level. The model considers four different failure modes: fibre rupture in tension, fibre buckling and kinking in compression, matrix cracking under transverse tension and shearing, and matrix crushing under transverse compression and shearing. This progressive damage model requires three essential components to be defined, including damage initiation criterion, damage evolution response, and damage stabilisation scheme.

According to the Hashin model, when the damage initiation criterion is met for any of the four failure modes, the damage variable for that failure mode is calculated as [50]:

$$d = \frac{\delta^{f}{}_{eq}(\delta_{eq} - \delta^{o}{}_{eq})}{\delta_{eq}(\delta^{f}{}_{eq} - \delta^{o}{}_{eq})} \qquad (1)$$

Where δ_{eq} is the equivalent displacement of the element as a function of its strain and characteristic length (square root of the area for shell elements). Abaqus uses this representation to alleviate the mesh dependency in strain-softening (progressive failure) cases. It expresses the softening part of the constitutive model as a stress-displacement $(\sigma - \delta)$ relation rather than the mesh dependent stress-strain $(\sigma - \varepsilon)$ model. $\delta^{o}{}_{eq}$ is the equivalent displacement at damage initiation and $\delta^{f}{}_{eq}$ is the equivalent displacement when the element is completely damaged. Fig. 3 depicts the above equation graphically, where the maximum value of the damage variable is 1.

The lamina strength limits used in this study are for unidirectional E-glass/Vinyl-Ester composites, shown in Table 4; these limits were extracted from [34] for the same profiles. After any damage initiation criterion is met within any element, the damage evolution algorithm for that damage mode works to simulate the progressive damage in that element. The damage evolution for fibre-reinforced materials is based on energy dissipation to trace the damage process. Thus, for each failure mode, the fracture energy which equals the area under the equivalent stress-displacement diagram of the element, must be specified. Due to the lack of experimental data on the fracture energy of E-glass/Vinyl-ester lamina for each failure mode, fracture energy values of E-glass/Ly556 epoxy lamina were used for the longitudinal tensile and compressive failure modes [56]. The transverse tensile and compressive fracture energy values were taken from [57] for numerical purposes for validation against the experimental data. The fracture energy values for the four failure modes of the lamina are shown in Table 4. These values obtained close FEM results to the experimental results of the structural profiles, as will be shown in the validation section.

Implicit solvers, such as Abaqus/Standard, usually present severe convergence difficulties when modelling material softening (failure) and stiffness degradation. To overcome this problem, Abaqus 2019 uses a viscous regularisation/stabilisation scheme to make the tangent stiffness matrix of the softening material positive for sufficiently time increments. The solver introduces a tangential viscous damage variable to the damage evolution equations [50]:

$$d'_v = \frac{1}{\eta}(d - d_v) \quad (2)$$

Where η is the viscosity coefficient which is used to relax the time in the vicious system, d and d_v are the damage variables evaluated in the inviscid and the viscous model, respectively. To specify the optimal viscosity coefficient values for the four failure modes, a sensitivity study with a range of $[1 \times 10^{-6} - 1 \times 10^{-3}]$ sec was performed on each PFRP profile geometry. After monitoring the study results and the energy balance of the models, a value of 1×10^{-3} sec was used as the viscosity coefficient for each failure mode for all profiles.

3.3 Mesh, boundary conditions, and loading condition

The PFRP profiles were modelled using 8-node quadrilateral in-plane general-purpose continuum shells (SC8R). This reduced integral 3D shell element with hourglass control and finite membrane strain forms the best option for both thick and thin shells. It allows through-thickness modifications such as tapering the geometry. It also provides more accurate visualisation and contact modelling than conventional shells and captures the through-thickness response more accurately [50]. A mesh sensitivity study was carried out to check the suitable element size allowing for results to converge. The mesh was enhanced by refining the number of elements through the thickness to capture the kinematic changes accurately and greatly reduce hourglass modes. A mesh with a 5 mm element edge length and five elements through-thickness was selected for S-100×100×5.2, S-125×125×6.4, and R-75×100×5.2 PFRP profiles. Since the corners form a critical zone for stress concentrations, five elements were locally assigned to each corner to refine the mesh. For the C1-89×6.0 and C2-89×6.0 PFRP profiles, a mesh with a 3 mm element edge length and five elements through-thickness was selected. For further details on the mesh sensitivity study and the element seeding, please refer to the supplementary data.

All the simulated profiles were assigned a fixed-fixed boundary condition on the ends. The top and bottom surfaces were restrained by preventing movement along their translational and rotational degrees of freedom in all directions. The axial translational movement at the profile top was allowed to simulate the axial compression through a displacement-control loading of 1 mm/min.

3.4 Modelling of local buckling

Since local buckling can be either symmetric or antisymmetric, it is preferred to model the full geometry of the structure without any symmetric boundary conditions [58–60]. Since the studied PFRP profiles have symmetric and balanced layups, coupling effects may appear at a bending-twisting form if symmetric boundary conditions are used [16,20,61].

One critical difficulty in modelling local buckling, in a time-incremental procedure, is that it results from a localised release of strain energy between neighbouring elements; consequently, resulting in a softening (degradation) of the structural stiffness. This release in the strain energy is because that part of the structure at the buckling point cannot maintain equilibrium. Thus, it releases a part of its strain energy via an out-of-plane deformation to maintain equilibrium under a new load path. This type of problem has to be modelled either dynamically or by the aid of artificial damping [14,30,52,62].

To simulate the localised release of strain energy and the need to include damping, the adaptive automatic stabilisation scheme in Abaqus/Standard is utilised in this study. Abaqus/Standard uses the Newton method to solve the nonlinear equations using a combination of incremental (dividing the step time) and iterative (attempting to find an equilibrium solution in the increment) procedures. Consequently, providing an excellent approach to simulate the nonlinearity accompanying local buckling. The adaptive automatic stabilisation scheme steadies unstable quasi-static problems by providing an automatic mechanism in which volume-proportional artificial damping is added to the model to stabilise the load-displacement path. The damping varies spatially and with time, along with the analysis duration, to account for stability changes. The damping value can be capped with a maximum value relative to the strain energy of the model. Thus, the effect of the artificial viscous damping energy (ALLSD) on the energy balance of the model can be controlled. By default, Abaqus/Standard specifies a value of 0.05 as a tolerance. This value means that the cap of the energy dissipated by viscous damping to the total strain energy is 5%. This value has proved to be suitable for this study. Moreover, the adaptive automatic stabilisation scheme is compatible with shell elements, as it facilitates the solution during the first increment when a poor estimation of the extrapolated strain energy might occur. For these reasons, the adaptive automatic stabilisation scheme in Abaqus/Standard is used in this approach for local buckling modelling.

The NLgeom (Nonlinear geometry) algorithm was implemented to permit for the usage of the large displacement formulation [19]. Thus, allowing to capture local buckling and the large displacements accompanying the post-peak behaviour [46].

In the Newton method, the total step time is divided into a number of increments. After each increment, the model stiffness matrix is updated. Modelling of stability-based behaviour, such as local buckling, is very sensitive to the maximum increment size assigned by the user (in the general static step definition tab) since the model stability is related to its stiffness matrix, which is updated relying on the number of increments [46]. As shown in Fig. 4 (a) for S-100×100×5.2 profile (L/D = 2), the maximum increment size had to be reduced to 0.35% of the total step time to reach convergence for the local buckling load capacity in the hollow box PFRP profiles. For all the simulated PFRP profiles, the recommended increment size range by Abaqus documentation (10% of the step time) was not sufficient. Thus, the maximum increment size had to be reduced until convergence is achieved with a percentile error of 5% between the load capacities of the successive increment sizes, as shown in Fig. 4 (b) for S-100×100×5.2 profile. The increment size sensitivity can be used to inspect the realistic failure mode. It is a good practice to initiate the analysis by two runs with maximum increment sizes of 10% and 5% of the step time, respectively. By doing that, compressive failure and local buckling failure modes can be differentiated. The load capacity of these two successive analyses will be the same if the dominant failure mode is compressive failure. Whereas, it will show a variation if local buckling occurred, as highlighted in Fig. 4. These two maximum increment sizes were chosen as a starting point since they will not consume high computational resources. Furthermore, if there is local instability, it will start appearing in the load-displacement path at one of them leaving the door open to seek convergence. This simplified approach alleviated the model's dependency on the increment size as a numerical parameter and obtained accurate results.

4. MODEL VALIDATION AND DISCUSSION

The validity and accuracy of the proposed modelling approach is assessed in the following sections. First, the FEM results were evaluated against the theoretical and experimental data in terms of the local buckling load capacity of the hollow box PFRP profiles. Second, the FEM load-displacement curves were compared to their experimental counterparts. Finally, the agreement in the mechanical properties and failure modes between the FEM and experimental results was studied. The data presented here on validation and discussion were used for illustration. For the complete validation, please refer to the supplementary data.

4.1 Local buckling load capacity of the hollow box PFRP profiles

The FEM results were compared to the current experimental results and data from the previous study [33] to examine the extent of agreement. Moreover, the most cited closed-form equations were used to estimate the local buckling loads (P_{cr}) of the hollow box PFRP profiles with L/D equals 2, as shown in Table 5. These equations assume clamped boundary conditions along the wall length and a uniaxial compressive loading along the wall width. The clamped boundary conditions assumption can be justified in this research by the high fibre volume fraction along the walls, interaction regions (corners), and the continuation of the inclined fibres around the corners [63]. Good agreement was found between these values. The S-125×125×6.4 profile exhibited a higher load capacity compared to the other profiles. This high load capacity is directly related to the larger cross-sectional area of the S-125×125×6.4 profile, which compensated for the slightly lower axial fibre content compared to the S-100×100×5.2 and R-75×100×5.2 profiles.

4.2 Load-displacement curves

The FEM analysis was performed in two phases in order to independently assess the proposed approaches individually, prior to assessing the combined effect. The adaptive automatic stabilisation scheme was studied first, followed by the addition of the progressive failure (Hashin damage) definition.

In the first phase, the adaptive automatic stabilisation scheme along with a controlled reduced incremental size and Nlgeom algorithm in Abaqus 2019 were implemented to capture the local buckling only without any failure definition. The models accurately captured the local buckling load in all of the hollow box PFRP profiles, as shown in Fig. 5 for the S-100×100×5.2 profile. The hollow circular profiles did not show local buckling effects. Overall, the hollow PFRP profiles exhibited linear elastic behaviour experimentally and numerically until the peak-point (maximum load point).

In the second phase, the same FEM models from the first phase were used along with the progressive failure (Hashin damage) definition. The FEM load-displacement curves matched the experimental results accurately for all the hollow PFRP profiles, as shown in Fig. 6 for the S-100×100×5.2 profile. Two out of the seven experimental curves of S-100×100×5.2 profile with L/D equals 2 (Fig. 6 (a)) had slightly eccentric results which caused a higher standard deviation in axial stiffness and strength, as shown in Table 6. It was inferred that these two profiles maybe defected. The hollow box profiles showed a post-peak behaviour prior to the final failure, while the hollow circular profiles failed sharply with no post-peak zone due to material compressive failure.

4.3 Mechanical properties

The FEM models obtained a strong agreement with the experimental data in terms of the axial compressive modulus and ultimate strength, as shown in Table 6. The axial stiffness (EA) of the hollow PFRP profiles is arranged ascendingly as follows: C2-89×6.0, C1-89×6.0, R-75×100×5.2, S-100×100×5.2, and S-125×125×6.4, as shown in Fig. 7 (a). C2-89×6.0 profile exhibited the least axial stiffness and elastic modulus since it has the lowest percentage of axial fibre and the largest inclined fibres angle. S-125×125×6.4 profile has a lower percentage of axial fibres compared to C1-89×6.0, R-75×100×5.2, and S-100×100×5.2 profiles. Nevertheless, it recorded the highest axial stiffness due to its larger cross-sectional area. R-75×100×5.2 profile represented the highest elastic modulus value, as shown in Fig. 7 (b), even though it has a similar percentage of axial fibres to S-100×100×5.2. This can be as attributed to the higher fibre volume fraction and lower inclined fibres angle in R-75×100×5.2.

When comparing the compressive strength of the hollow PFRP profiles, C1-89×6.0 then C2-89×6.0 circular profiles were highest, followed by R-75×100×5.2, as shown in Fig. 7 (b). This can be as attributed to the absence of local buckling in the circular profiles allowing for the full utilisation of their structural capacity, whereas the local buckling effect limited the R-75×100×5.2 profile due to the higher resistance to buckle in the shorter walls. On the other hand, S-100×100×5.2 profile had the least strength due to its thinner wall thickness compared to S-125×125×6.4 profile.

4.4 Failure mode

The failure mode of the axially loaded hollow PFRP profiles varied depending on their cross-sectional shape. The hollow box profiles were dominated by local buckling of the walls. Whereas the hollow circular profiles were dominated by compressive and shear failure at the profiles ends. The FEM failure modes closely agreed with the experimental observed behaviour.

The failure mode in the hollow box PFRP profiles started with local buckling at the peak-point, evident by the localised out-of-plane deformation/waves. As expected from the tested profiles, their low L/D ratio prevented the columns' axes from movement. Thus, global buckling was not experimentally observed nor numerically monitored. Just after the local buckling point (peak-point), the applied load encountered a sharp drop due to the sudden loss of stability. Subsequently, the hollow box PFRP profiles went through a post-peak phase, which became more evident when L/D ratio was increased, while for small L/D ratio, the post-peak zone diminished. This behaviour is addressed in the "Effect of Profile Slenderness Ratio" section. During the post-peak zone, the failure in the buckled profiles was initiated by shear, tensile, and compressive damage in the matrix at the waving regions due to the out-of-plane deformation. Afterwards, the localised waves subsided when the full profile collapse occurred due to compressive failure, in addition to localised tensile failure in fibres at the mid-height of the profile's wall. Fig. 8 shows the failure sequence of S-100×100×5.2 profile with L/D equals 3.5 illustrated by matrix (resin) tensile failure counters to highlight the localised waves propagation, which is compared to the experimental buckled shape at the same time increment.

The R-75×100×5.2 profile had a shorter sharp drop, after the local buckling point, in the load-displacement curves compared to S-100×100×5.2 and S-125×125×6.4 profiles. It can be inferred that the different cross-sectional aspect ratio (wall height/wall width) of R-75×100×5.2 profile helped in a fast recovery of the stability since the 75 mm walls need a higher load to buckle compared to the 100 mm walls. Thus, after the 100 mm walls buckled, the 75 mm walls were still resisting the loads and maintained a higher loading level after buckling compared to the hollow square PFRP profiles.

It is worth mentioning that delamination between plies was not modelled due to computational limitations. Since the current FEM modelling approach closely matched the experimental and theoretical results, it can be concluded that delamination is not dominant in the hollow PFRP profiles until the entire collapse of the profiles occurs. This is because of the high confinement in the PFRP profiles due to the closed geometry and the continuous inclined fibres layup that wrap the axial plies. Nevertheless, since transverse shear and tensile damage in the matrix can provide an indication of delamination propagation [20], tracking these failure modes can assess the models' capability of capturing the experimental failure mode, which is represented by ply splitting, after the post-peak region. The output variable (DAMAGESHR) in Abaqus/CAE can be used to reflect these effects. Based on that, the FEM models showed a good agreement with the experimental failure mode, as shown in Fig. 9 for S-100×100×5.2 profile with L/D ratio equals 5.0 for example.

Regarding the hollow circular PFRP profiles, the failure mode was the same for all L/D ratios. The failure was characterised by crushing at the profiles ends due to compressive damage in fibres accompanied by matrix shear failure, as shown in Fig. 10 for C2-89×6.0 profile with L/D equals 5.0. This failure mode was similar to what was reported in Reference [22].

5. INTERPRETATION OF THE NUMERICAL LOCAL BUCKLING AND FAILURE OBSERVATIONS

After validating the FEM models, their numerical results were used to explain two events that were not clear in the experimental data. The first observation was related to the peak-point and the post-peak behaviour of the hollow box PFRP profiles. These behaviours were addressed using the energy parameters of the numerical models. The second observation was the effect of the column slenderness ratio on its behaviour. The data presented here on these observations were used for illustration. For the complete dataset, please refer to the supplementary data.

5.1 Energy parameters

With validated models, the energy outputs provide valuable information regarding the peak-point and post-peak behaviours. The strain energy was used to address the local buckling behaviour, while the damage dissipation energy was used to trace the progressive failure.

5.1.1 Strain energy

The strain energy is an essential factor to be studied when characterising the structural behaviour of loaded members since the member load-carrying pattern is a reflection of the strain energy storage and release. If the release in the strain energy is minor (localised) and followed by a storing process, then it can indicate the models response to a local instability (e.g. local buckling) by changing its loading path to maintain equilibrium [14,30,50]. Fig. 11 shows the strain energy and load values vs the axial displacement of S-100×100×5.2 profile with L/D ratio equals 5. It is obvious that the extent of the post-peak zone changes along with the L/D ratio. For small L/D ratio, the post-peak zone diminishes, and its restored strain energy as well. While for a higher L/D ratio, the post-peak zone and its resorted strain energy become clear. It is evident that the amount of the restored strain energy at the post-peak zone controls its behaviour, as shown in

Fig. 12, which presents the resorted strain energy at the post-peak zone vs L/D ratio for the hollow box PFRP profiles. S-100×100×5.2 profile exhibited the highest restoration capability followed by R-75×100×5.2, then S-125×125×6.4 profiles when L/D ratio is increased. In other words, S-100×100×5.2 profile showed larger relative deformation after buckling than other profiles evident by the larger axial shortening after buckling. This was referred to the lower wall thickness it has compared to S-125×125×6.4 profile, which resulted in a lower axial stiffness against deformations. Compared to R-75×100×5.2 profile, the walls of S-100×100×5.2 are wider, which resulted in a longer unstiffened length for more out-of-plane deformation after buckling.

5.1.2 Damage index

The damage dissipated energy of the model due to the failure of the constituents on the element level is another vital energy output that provides informative signs regarding the progressive failure status. It was normalised in this study to introduce a Damage Index (DI) parameter, which provides a percentage of damage in the model along the test time, as follows:

$$Damage\ Index\ (DI) = \frac{Damage\ disspation\ energy\ at\ time\ (t)}{Total\ damage\ disspation\ energy} \times 100\% \qquad (3)$$

Fig. 13 shows the DI and load vs axial displacement for the S-100×100×5.2 profile with L/D equal to 5. The post-peak zone for high L/D ratios has a very small DI compared to the following failure zone. This small damage can be attributed to the matrix tensile and compressive crack initiation due to the localised out-of-plane deformation of the walls accompanying local buckling. On the other hand, the hollow circular profiles witnessed a sharp jump in DI value just after the peak-point. This jump is accompanied by a severe drop in the load-carrying capacity.

Since these profiles were not affected by local buckling, their compressive failure in fibres and shear failure in the matrix were sudden and drastic.

5.2 Effect of profile slenderness ratio

5.2.1 Hollow box PFRP profiles

Previous studies confirmed that the local buckling load capacity decreases and the number of localised waves increases when the L/D ratio is increased [1,14,20,60,64]. This is clear from the tested hollow box PFRP profiles, as shown in Fig. 14 (a) for S-100×100×5.2 profile. Increasing L/D ratios resulted in a reduction of the axial stiffness, as it increased the unsupported length of the profiles as reported by [1,20,65].

It is also evident that the post-peak zone extent is increasing when L/D ratio is increased. This behaviour can be explained using the normalised strain energy for each L/D ratio for each profile, as shown in Fig. 14 (b) for S-100×100×5.2 profile, which demonstrates the normalised strain energy vs test time for each L/D ratio. It can be concluded that for small L/D ratios, the normalised strain energy is higher at the local buckling point as it is being stored in a fewer number of localised waves. Thus, the post-peak zone will be infinitesimal because the damage evolution criteria are met just after the local buckling point due to this high normalised strain energy. On the other hand, for high L/D ratio, the normalised strain energy is lower at the local buckling point as it is being stored in a higher number of localised waves. Thus, the post-peak zone will be visible because the damage evolution criteria just after the local buckling point need more strain energy to be met.

After the post-peak zone, the effect of L/D ratio on the failure of the hollow box PFRP profiles was studied by assessing the density of each failure mode of the constituents. These failure modes are referring to the damage progression in fibres by compression (DAMAGEFC), in fibres by tension (DAMAGEFT), in the matrix by compression (DAMAGEMC), in the matrix by tension (DAMAGEMT), and in the matrix by shear (DAMAGESHR). The density of each failure mode, represented by the number of failed elements, at each L/D ratio for S-100×100×5.2 profile is shown in Fig. 15 (a). For all L/D ratios, the density of matrix failure by tension, compression, and shear is higher than that for fibres failure by compression and tension. This can be referred to as the lower strength limits and fracture energy of the matrix compared to the fibres. In addition, as L/D ratio is increasing, the densities of fibre failure by compression and tension are nearly constant. While the densities of matrix failure by compression, tension, and shear are increased. It can be inferred that the higher number of localised waves (delamination zones) when increasing L/D ratio is the reason. Consequently, matrix failure is extending across these zones when L/D is increased and causing an increase in the relevant densities.

5.2.2 Hollow circular PFRP profiles

Regarding the hollow circular profiles, the load capacity was equivalent across all L/D ratios since they did not experience local buckling. Moreover, the axial shortening increased, and the axial stiffness decreased when L/D ratio is increased, as shown in Fig. 16 (a) for C1-89×6.0 profile.

Since the hollow circular profiles failed by compressive failure, their normalised strain energy across different L/D ratios was constant, as shown in Fig. 16 (b) for C1-89×6.0 profile. It can be concluded that the damage evolution criteria were met at the same part of the profiles (the ends of the profiles) across all L/D ratios. Thus, the same amount of normalised strain energy was stored in these profiles.

Fig. 15 (b) shows the failure modes densities versus L/D ratios for C1-89×6.0 profile. The fibre damage by tension and the matrix damage by compression have negligible densities. There is no tensile damage in fibres since they are subjected to compression loading. The matrix has a lower tensile strength than compression. Thus, it fails by transverse tensile cracks before the compression failure criterion is satisfied. Moreover, when L/D ratio is increased, the other failure densities remain nearly constant. This can be referred to as the constant failure zone (the ends of the profiles) across all L/D ratios.

6. CONCLUSIONS

A nonlinear buckling analysis approach has been developed in this research using an incremental analysis in Abaqus/Standard (2019). An extensive experimental program consisting of 44 specimens was undertaken to validate this modelling approach under axial compression. The FEM results had good agreement with the theoretical results and closely agreed with experimental results and literature data. The proposed methodology presents a helpful utility to design and optimise the PFRP profiles against local buckling and compressive failure. It can also help in analysing and studying the effect of many design parameters on these profiles in early design stages to enhance their strength and stiffness properties. From this study, the following points were concluded:

- The proposed FEM modelling approach using Abaqus 2019 proved its accuracy against theoretical, experimental, and published data. The incremental approach using the Newton method along with the adaptive automatic stabilisation scheme and the controlled increment size demonstrated its accuracy and validity to undertake a nonlinear geometric analysis of local buckling in PFRP profiles. The progressive failure based on Hashin damage criteria proved to be a very accurate and useful tool to investigate the load capacity and compressive failure in PFRP profiles. Overall, the proposed FEM approach represents a simple and robust utility to model and investigate the mechanical behaviour of PFRP profiles. The energy parameters and constituent failure modes of the FEM models helped greatly in explaining the effect of the dimensions, layups, and slenderness ratios on the failure modes of the PFRP profiles.

- The failure in the hollow box profiles was triggered by local buckling. When the length-to-width (L/D) ratio is increased, the local buckling capacity of the hollow box PFRP profiles decreases. On the other hand, the load capacity of the hollow circular PFRP profiles remains constant when changing L/D ratio. These profiles were dominated by compressive failure as their strength limit was reached. Both cross-sectional shapes exhibited linear elastic behaviour and degradation in the axial stiffness when L/D is increased.
- For the hollow box profiles, the post-peak zone after local buckling becomes more evident when the L/D ratio is increased. It was inferred that the larger number of localised waves distributed the damage over a larger zone and resulted in lower normalised strain energy when the L/D ratio is increased. Consequently, allowing for a higher restoration in the strain energy, causing the post-peak zone to extend further. Contrary, the hollow circular profiles exhibited a sharp drop in their load-displacement curves just after their load capacity is reached.
- Increasing the inclined fibre content results in higher circumferential confinement and a larger transverse deformation tolerance before failure or buckling. Consequently, this led to a higher overall axial shortening in the elastic zone as seen for C2-89×6.0 and S-125×125×6.4 profiles compared to C1-89×6.0 and the other hollow box profiles, respectively. However, these profiles exhibited lower axial modulus compared to their counterparts. On the other hand, profiles with lower wall thickness showed a higher strain energy restoration after buckling and a larger axial shortening after buckling due to the lower axial stiffness of the buckled walls as seen in S-100×100×5.2 and R-75×100×5.2 profiles.
- After the post-peak zone, the failure in the hollow box PFRP profiles was characterised by fibre compressive failure and localised fibre tensile rupture at the profiles mid-height. In

addition to that, matrix compressive, tensile, and shear failure occurred along the profile at the localised waving zones. While the fibres failure densities were constant when L/D ratio is increased, the matrix failure densities increased in a sign to the larger growth of delamination zones as the unsupported length is increased. Regarding the hollow circular profiles, the densities of compressive failure in fibres and shear failure in the matrix were constant when L/D ratio is increased. This is because the failure occurred along an invariant failure zone at the profile's ends.

Further investigations would be required to assess and enhance the proposed FEM modelling approach to extend it to cover higher L/D ratios and more loading conditions such as bending and shear. Consequently, allowing for the capture of interactions with other buckling types, such as global flexural buckling and lateral-torsional buckling.

ACKNOWLEDGEMENTS

The work was funded through a Cooperative Research Centres Projects (CRC-P) Grant (CRCPSIX000117). Acknowledgement is also given to Dr. Rajab Abousnina for his assistance in conducting the experimental tests.

REFERENCES

[1] Bank LC. Composites for Construction: Structural Design with FRP Materials. John Wiley & Sons; 2006.

[2] Singer J, Arbocz J, Weller T, Cheney JA. Buckling Experiments: Experimental Methods in Buckling of Thin-Walled Structures. Shells, Built-up Structures, Composites and Additional Topics, Volume 2. Appl Mech Rev 2003;56:B5.

[3] Guades E, Aravinthan T, Islam M, Manalo A. A review on the driving performance of FRP composite piles. Compos Struct 2012;94:1932–42. https://doi.org/10.1016/j.compstruct.2012.02.004.

[4] Fangueiro R. Fibrous and Composite Materials for Civil Engineering Applications. Elsevier; 2011.

[5] Jones RM. Mechanics Of Composite Materials. CRC Press; 1998.

[6] Uddin N. Developments in Fiber-Reinforced Polymer (FRP) Composites for Civil Engineering. Elsevier; 2013.

[7] Kaw AK. Mechanics of Composite Materials. CRC Press; 2005.

[8] Balasubramanian M. Composite Materials and Processing. CRC Press; 2013.

[9] GAJJAR D. Development of applications and innovation of FRP Pultruded Profiles in India & Asia 2020.

[10] Sapuan SM. Composite Materials: Concurrent Engineering Approach. Butterworth-Heinemann; 2017.

[11] Vinson JR, Sierakowski RL. The Behavior of Structures Composed of Composite Materials. Springer; 2006.

[12] Bunsell AR, Renard J. Fundamentals of Fibre Reinforced Composite Materials. CRC Press; 2005.

[13] Oller S. Numerical simulation of mechanical behavior of composite materials. 1. ed. Barcelona: Springer; 2014.

[14] Attaf B. Advances in Composite Materials: Ecodesign and Analysis. BoD – Books on Demand; 2011.

[15] Buragohain MK. Composite Structures: Design, Mechanics, Analysis, Manufacturing, and Testing. CRC Press; 2017.

[16] Department of Defense. Composite materials handbook, volume 3: polymer matrix composites—materials usage, design and analysis. SAE International; 2002.

[17] Matthews FL, Davies GAO, Hitchings D, Soutis C. Finite Element Modelling of Composite Materials and Structures. Elsevier; 2000.

[18] Singer J, Arbocz J, Weller T. Buckling Experiments: Experimental Methods in Buckling of Thin-Walled Structures Shells, Built-up Structures, Composites and Additional Topics. vol. 2. 2002.

[19] Xu J, Zhao Q, Qiao P. A critical review on buckling and post-buckling analysis of composite structures. Front Aerosp Eng 2013;2:157–168.

[20] Barbero EJ. Introduction to Composite Materials Design. CRC Press; 2017. https://doi.org/10.1201/9781315296494.

[21] Cardoso DCT, Harries KA, Batista E de M. Compressive strength equation for GFRP square tube columns. Compos Part B Eng 2014;59:1–11. https://doi.org/10.1016/j.compositesb.2013.10.057.

[22] Wang W, Sheikh MN, Hadi MNS. Behaviour of perforated GFRP tubes under axial compression. Thin-Walled Struct 2015;95:88–100. https://doi.org/10.1016/j.tws.2015.06.019.

[23] Aleksendric D, Carlone P. Soft Computing in the Design and Manufacturing of Composite Materials: Applications to Brake Friction and Thermoset Matrix Composites. Woodhead Publishing; 2015.

[24] Gibson RF. Principles of Composite Material Mechanics. CRC Press; 2016.

[25] Mallick PK. Fiber-reinforced composites: materials, manufacturing, and design. CRC press; 2007.

[26] Najafi A, Rais-Rohani M. Concurrent Process-Product Design Optimization Using Coupled Nonlinear Finite-Element Simulations. Finite Elem Anal - Appl Mech Eng 2012. https://doi.org/10.5772/47852.

[27] Rammerstorfer FG. ENGINEERING MECHANICS OF FIBRE REINFORCED POLYMERSAND COMPOSITE STRUCTURES. Springer; 1994.

[28] Soares CAM, Soares CMM, Freitas MJM. Mechanics of Composite Materials and Structures. Springer Science & Business Media; 2013.

[29] Vasiliev VV, Morozov EV. Advanced Mechanics of Composite Materials and Structures. Elsevier; 2018.

[30] Barbero EJ. Finite Element Analysis of Composite Materials using AbaqusTM. CRC Press; 2013.

[31] Sayyad AS, Ghugal YM. Bending, buckling and free vibration of laminated composite and sandwich beams: A critical review of literature. Compos Struct 2017;171:486–504. https://doi.org/10.1016/j.compstruct.2017.03.053.

[32] Kreja I. A literature review on computational models for laminated composite and sandwich panels. Cent Eur J Eng 2011;1:59–80.

[33] Al-saadi AU, Aravinthan T, Lokuge W. Effects of fibre orientation and layup on the mechanical properties of the pultruded glass fibre reinforced polymer tubes. Eng Struct 2019;198:109448. https://doi.org/10.1016/j.engstruct.2019.109448.

[34] Al-Saadi A, Aravinthan T, Lokuge W. Numerical Investigation on Hollow Pultruded Fibre Reinforced Polymer Tube Columns. ACMSM25, Springer; 2020, p. 455–465.

[35] Guades E, Aravinthan T, Islam MM. Characterisation of the mechanical properties of pultruded fibre-reinforced polymer tube. Mater Des 2014;63:305–15. https://doi.org/10.1016/j.matdes.2014.06.018.

[36] Aktaş M, Balcıoğlu HE. Buckling behavior of pultruded composite beams with circular cutouts. Steel Compos Struct 2014;17:359–370.

[37] Doan QH, Thai D-K, Tran NL. A Numerical Study of the Effect of Component Dimensions on the Critical Buckling Load of a GFRP Composite Strut under Uniaxial Compression. Materials 2020;13:931. https://doi.org/10.3390/ma13040931.

[38] Noh J, Ghadimi B, Russo S, Rosano M. Assessment of FRP pultruded elements under static and dynamic loads. Compos Struct 2018;202:17–28. https://doi.org/10.1016/j.compstruct.2017.09.107.

[39] Qiao Pizhong, Zou Guiping. Local Buckling of Composite Fiber-Reinforced Plastic Wide-Flange Sections. J Struct Eng 2003;129:125–9. https://doi.org/10.1061/(ASCE)0733-9445(2003)129:1(125).

[40] Szklarek K, Gajewski J, Valis D. Estimation of critical force of the buckling composite structures using modelling methods. MATEC Web Conf., vol. 252, EDP Sciences; 2019, p. 03004.

[41] Szymczak C, Kujawa M. Local buckling of composite channel columns. Contin Mech Thermodyn 2018:1–13.

[42] Tang J, Chen X, Yang K. Evaluating Structural Failure of Load-Carrying Composite Box Beams with Different Geometries and Load Conditions. Appl Compos Mater 2019;26:1151–61. https://doi.org/10.1007/s10443-019-09776-4.

[43] Almeida JHS, Tonatto MLP, Ribeiro ML, Tita V, Amico SC. Buckling and post-buckling of filament wound composite tubes under axial compression: Linear, nonlinear, damage and experimental analyses. Compos Part B Eng 2018;149:227–39. https://doi.org/10.1016/j.compositesb.2018.05.004.

[44] Chawla H, Singh SB. Stability and failure characterization of fiber reinforced pultruded beams with different stiffening elements, part 2: Analytical and numerical studies. Thin-Walled Struct 2019;141:606–26. https://doi.org/10.1016/j.tws.2018.10.024.

[45] Correia M. M., Nunes F., Correia J. R., Silvestre N. Buckling Behavior and Failure of Hybrid Fiber-Reinforced Polymer Pultruded Short Columns. J Compos Constr 2013;17:463–75. https://doi.org/10.1061/(ASCE)CC.1943-5614.0000339.

[46] Turvey GJ, Zhang Y. A computational and experimental analysis of the buckling, postbuckling and initial failure of pultruded GRP columns. Comput Struct 2006;84:1527–37. https://doi.org/10.1016/j.compstruc.2006.01.028.

[47] Debski H, Rozylo P, Gliszczynski A, Kubiak T. Numerical models for buckling, postbuckling and failure analysis of pre-damaged thin-walled composite struts subjected to uniform compression. Thin-Walled Struct 2019;139:53–65. https://doi.org/10.1016/j.tws.2019.02.030.

[48] Hassan NK, Mosallam AS. Buckling and ultimate failure of thin-walled pultruded composite columns. Polym Polym Compos 2004;12:469–481.

[49] Khakimova R, Castro SGP, Wilckens D, Rohwer K, Degenhardt R. Buckling of axially compressed CFRP cylinders with and without additional lateral load: Experimental and numerical investigation. Thin-Walled Struct 2017;119:178–89. https://doi.org/10.1016/j.tws.2017.06.002.

[50] Simulia DS. Abaqus 6.13 Analysis User's Guide. Dassault Syst Provid RI 2013.

[51] Boscato G, Casalegno C, Russo S. Performance of built-up columns made by pultruded FRP material. Compos Struct 2015;121:46–63. https://doi.org/10.1016/j.compstruct.2014.11.022.

[52] Kobayashi T, Mihara Y. Application of Abaqus for Practical Postbuckling Analyses of Cylindrical Shells under Axial Compression, Providence, Rhode Island: Dassault Systemes, 2010; 2010.

[53] Vaziri A. On the buckling of cracked composite cylindrical shells under axial compression. Compos Struct 2007;80:152–8. https://doi.org/10.1016/j.compstruct.2006.05.007.

[54] Tafreshi A, Oswald T. Global buckling behaviour and local damage propagation in composite plates with embedded delaminations. Int J Press Vessels Pip 2003;80:9–20. https://doi.org/10.1016/S0308-0161(02)00152-7.

[55] Daniel IM, Ishai O. Engineering Mechanics of Composite Materials. Oxford University Press; 2006.

[56] Sharma AP, Khan SH, Parameswaran V. Experimental and numerical investigation on the uni-axial tensile response and failure of fiber metal laminates. Compos Part B Eng 2017;125:259–74. https://doi.org/10.1016/j.compositesb.2017.05.072.

[57] Tarfaoui M, El Moumen A, Lafdi K. Progressive damage modeling in carbon fibers/carbon nanotubes reinforced polymer composites. Compos Part B Eng 2017;112:185–95. https://doi.org/10.1016/j.compositesb.2016.12.056.

[58] Eslami MR. Buckling and Postbuckling of Beams, Plates, and Shells. Springer; 2017.

[59] Timoshenko SP, Gere JM. Theory of Elastic Stability. Dover Publications, Inc.; 1961.

[60] Turvey GJ, Marshall IH. Buckling and Postbuckling of Composite Plates. Springer Science & Business Media; 1995.

[61] Butler R, Rhead A, Dodwell T. 8.7 Optimum Design and Damage Tolerance of Compressively Loaded Laminates. In: Beaumont PWR, Zweben CH, editors. Compr. Compos. Mater. II, Oxford: Elsevier; 2018, p. 118–35. https://doi.org/10.1016/B978-0-12-803581-8.10060-8.

[62] Boulbes RJ. Troubleshooting Finite-Element Modeling with Abaqus. Springer; 2020.

[63] Regel F. A modelling approach for 3D braid reinforced composites under non-axial loading. PhD Thesis. University of Minho, 2014.

[64] Abramovich H. Stability and Vibrations of Thin-Walled Composite Structures. Woodhead Publishing; 2017.

[65] Kollár LP, Springer GS. Mechanics of Composite Structures. Cambridge University Press; 2003.

[66] Ascione L, Caron J-F, Godonou P, van Ijselmuijden K, Knippers J, Mottram T, et al. Prospect for new guidance in the design of FRP : Support to the implementation, harmonization and further development of the Eurocodes. Publications Office of the European Union; 2016.

FIGURES

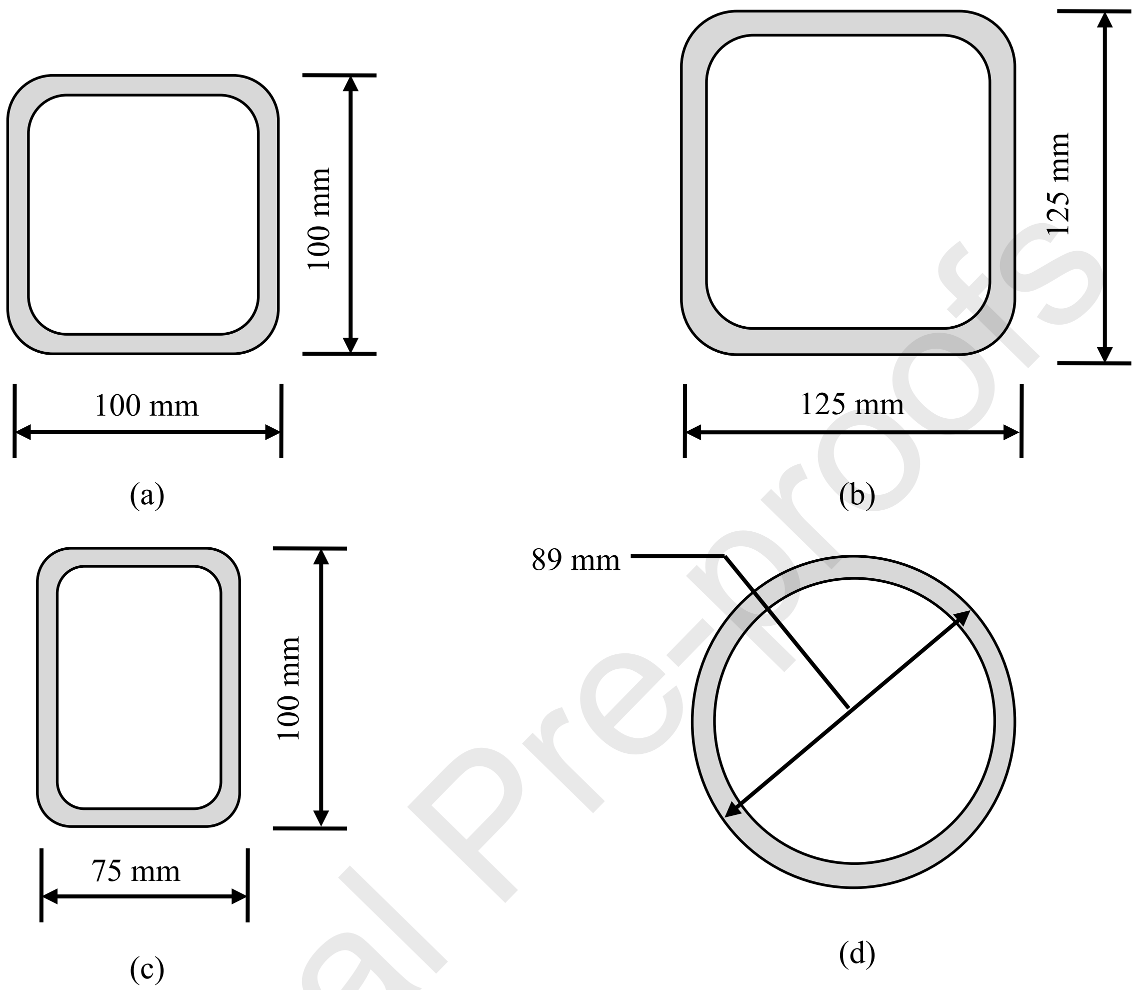

Fig. 1. Cross-sectional dimensions of the hollow PFRP profiles (a) S-100×100×5.2 (b) S-125×125×6.4 (c) R-75×100×5.2 and (d) C-89×6.0.

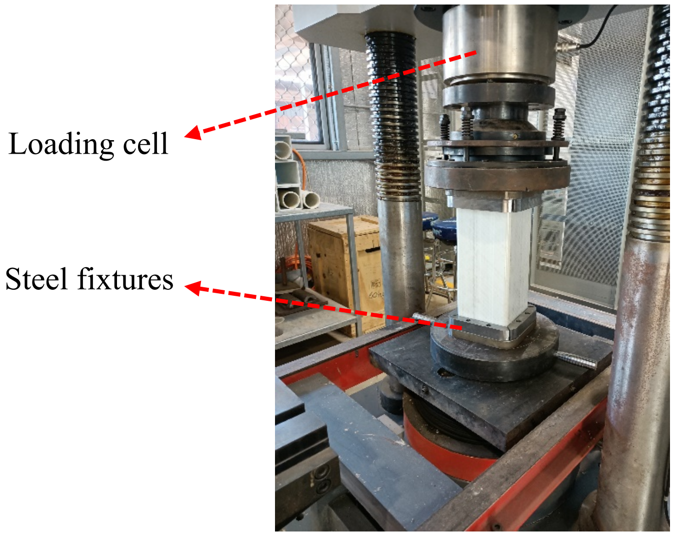

Fig. 2. Testing SANS machine loaded with a PFRP specimen.

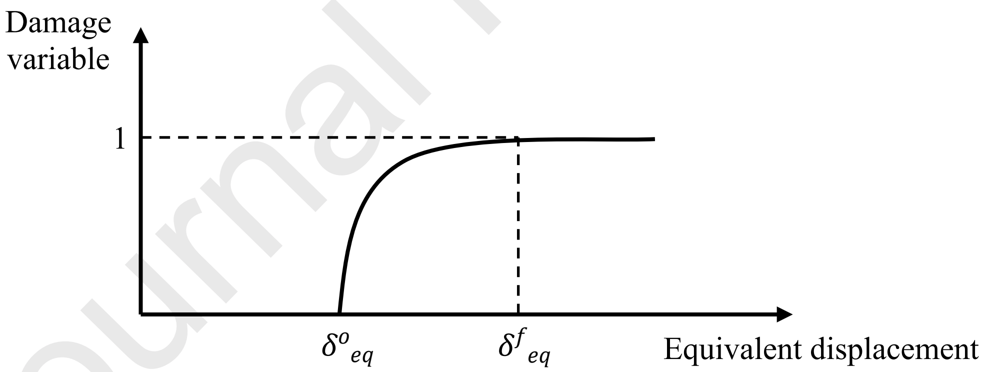

Fig. 3. Damage variable as a function of equivalent displacement [50].

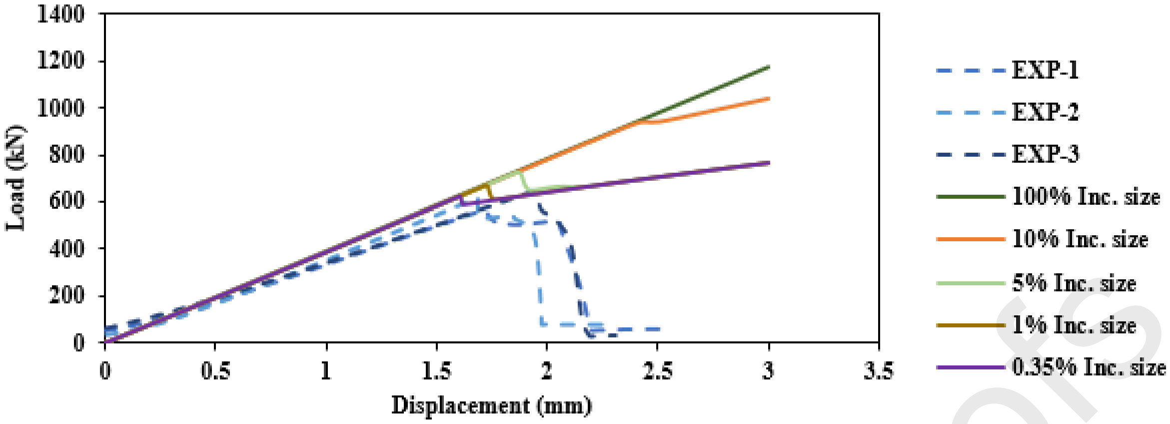

(a)

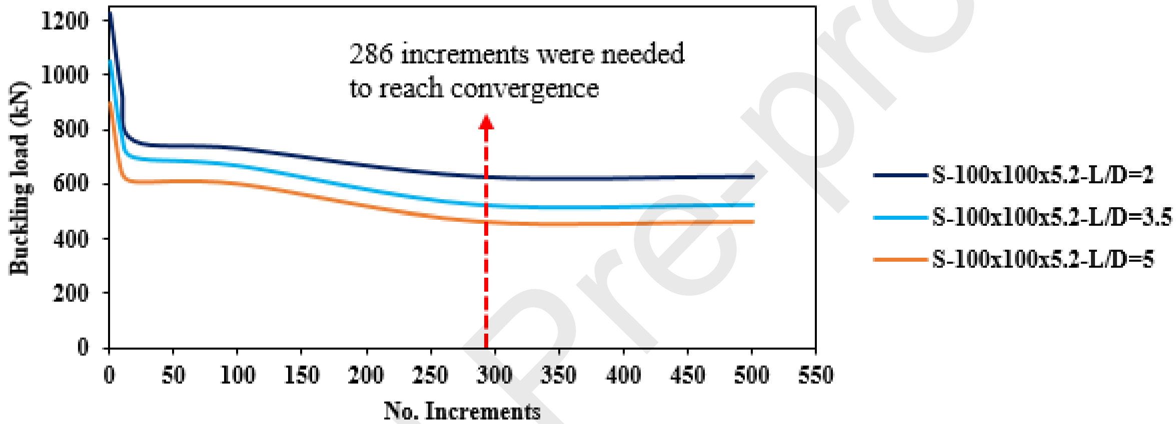

(b)

Fig. 4. Local buckling load convergence when reducing the increment size for S-100×100×5.2 PFRP profile (a) experimental vs numerical load-displacement curves with L/D equals 2 and (b) convergence curves for all L/D ratios.

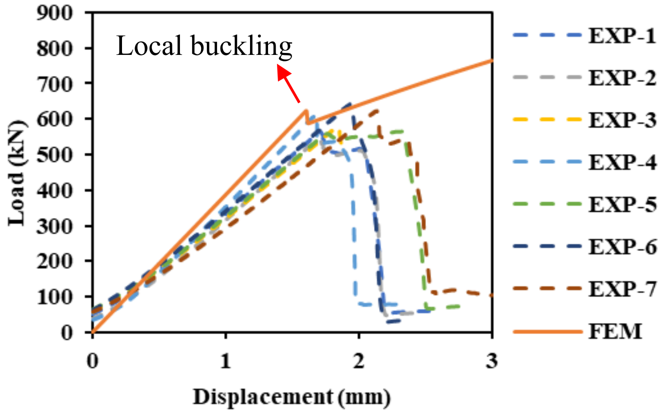

(a)

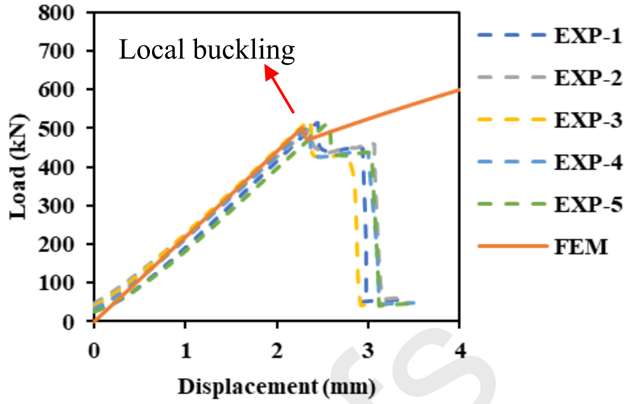

(b)

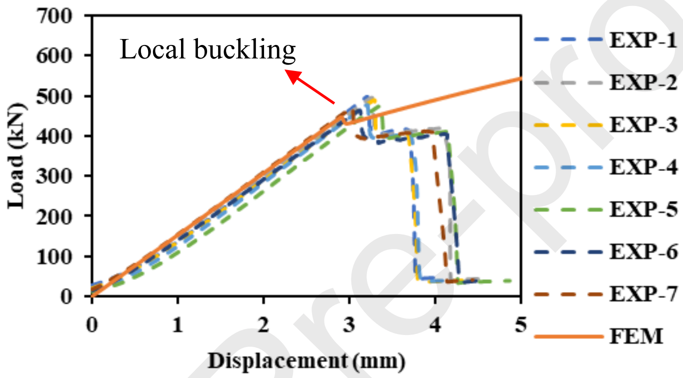

(c)

Fig. 5. Phase one FEM vs experimental load-displacement curves for S-100×100×5.2 profile with L/D equals (a) 2 (b) 3.5 and (c) 5.

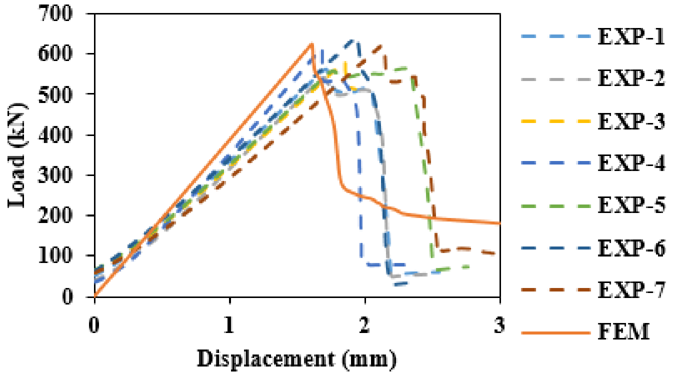

(a)

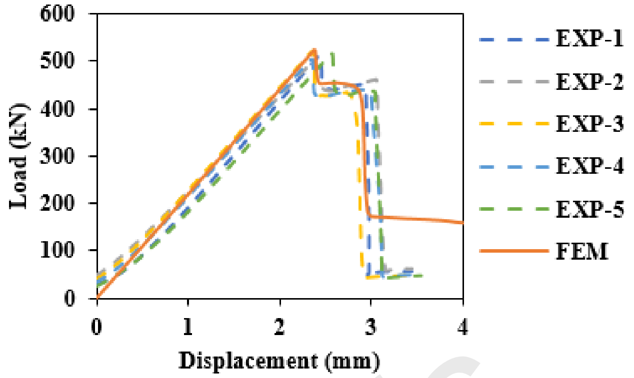

(b)

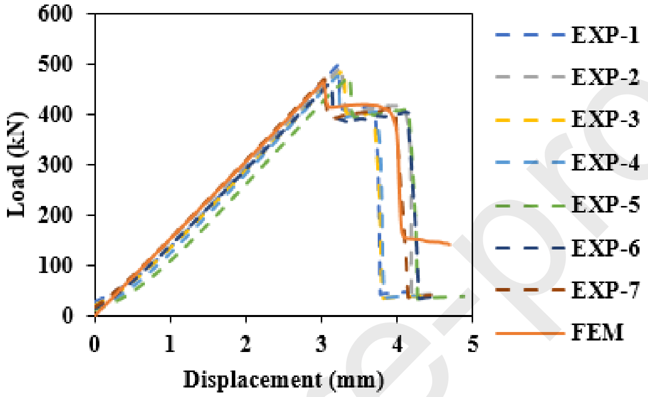

(c)

Fig. 6. Phase two FEM vs experimental load-displacement curves for S-100×100×5.2 profile with L/D equals (a) 2 (b) 3.5 and (c) 5.

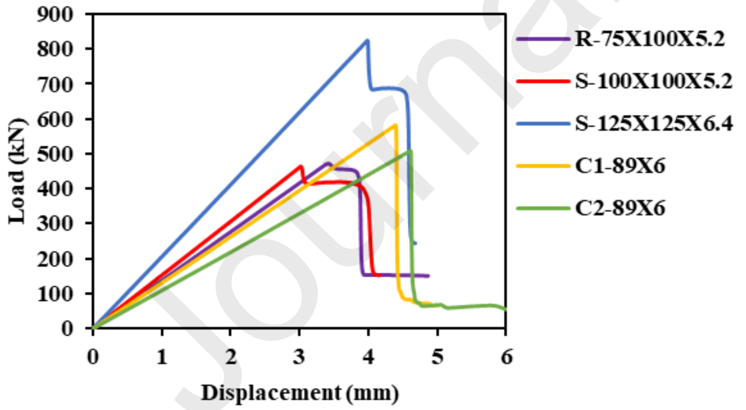

(a)

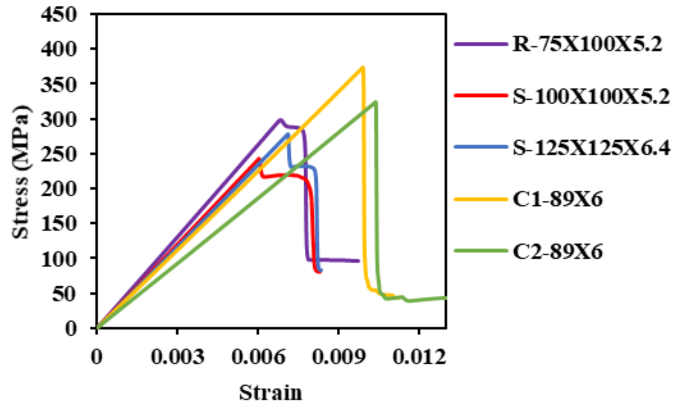

(b)

Fig. 7. Mechanical properties of the hollow PFRP profiles with L/D equals 5 (a) load-displacement and (b) axial stress-strain curves.

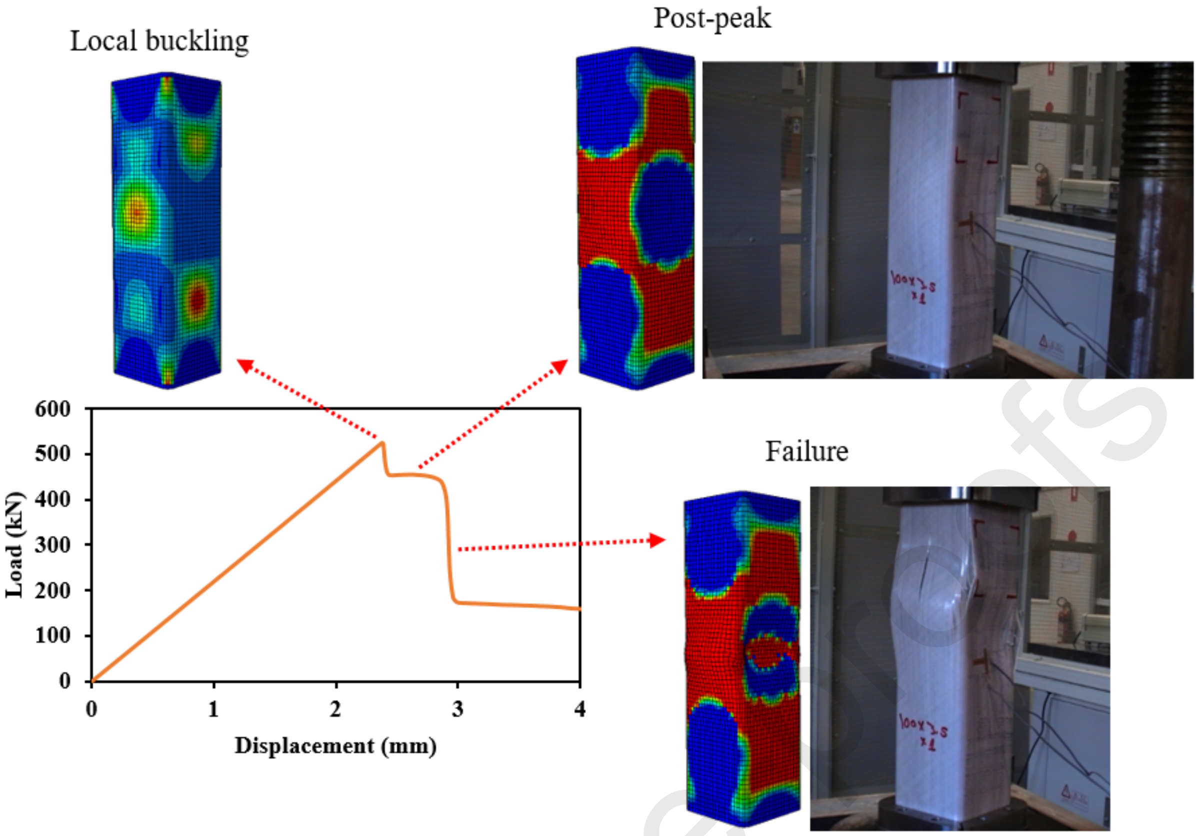

Fig. 8. Failure sequence in S-100×100×5.2 hollow box PFRP profile with L/D equals 3.5.

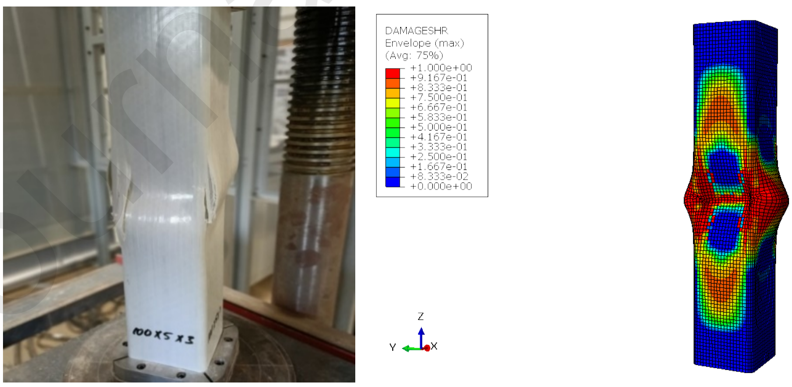

(a) (b)

Fig. 9. Failure mode of S-100×100×5.2 profile with L/D ratio equals 5 (a) Experimental vs (b) FEM.

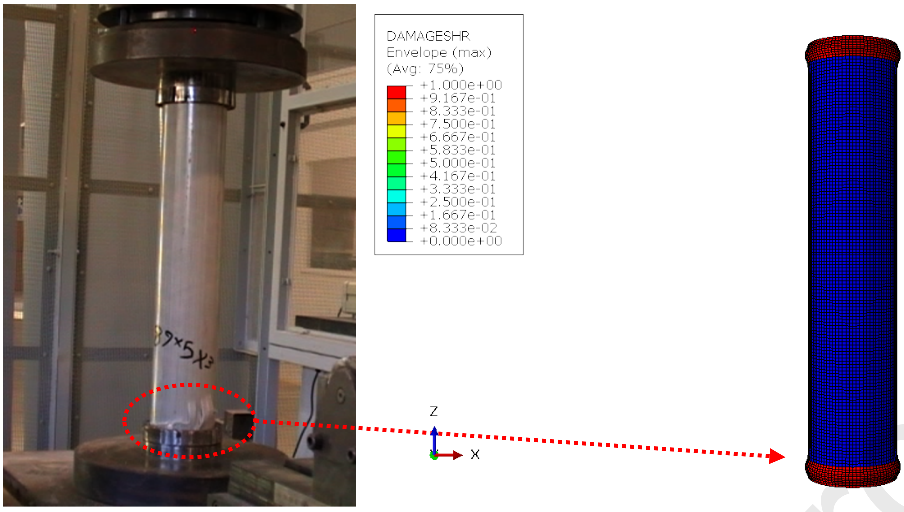

(a) (b)

Fig. 10. Failure mode of hollow circular profile C2-89×6.0 with L/D ratio equals 5 (a) Experimental vs (b) FEM.

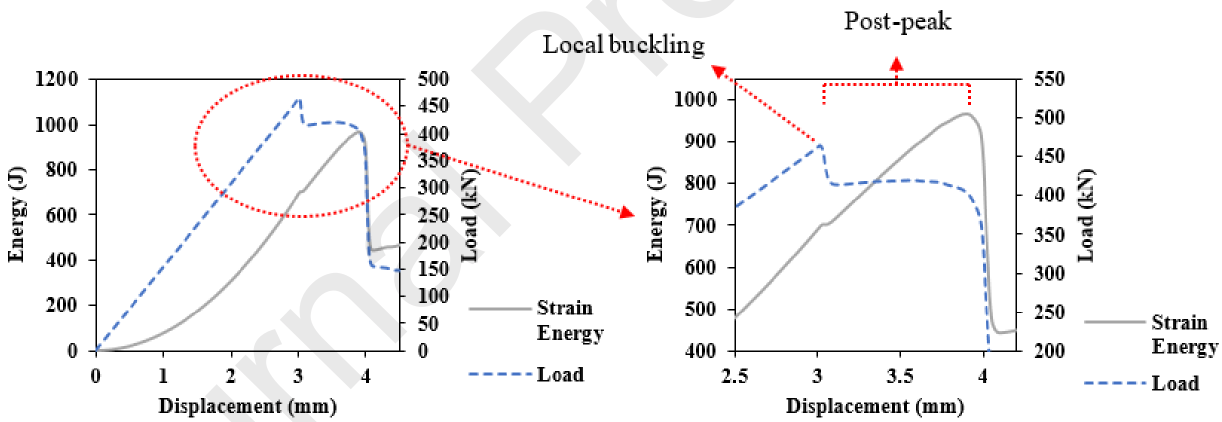

Fig. 11. Strain energy and load values vs the axial displacement of S-100×100×5.2 profile with L/D equals 5.

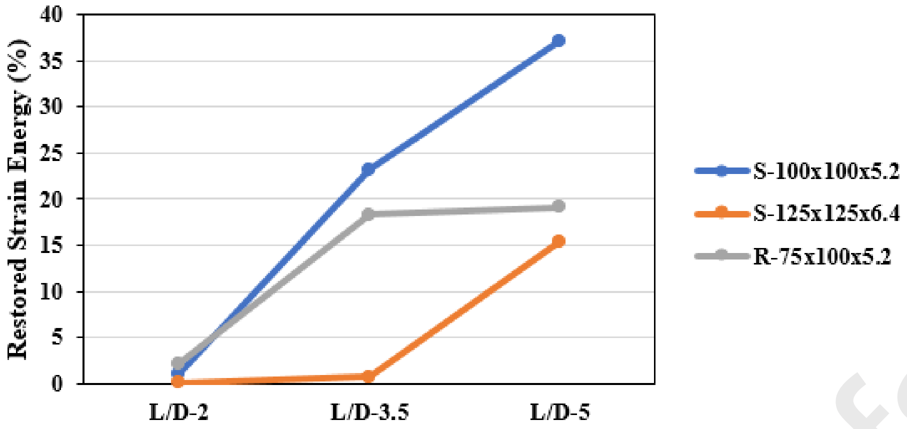

772

773 *Fig. 12. Resorted strain energy at the post-peak zone vs L/D ratio for the hollow box PFRP profiles.*

774

775

776

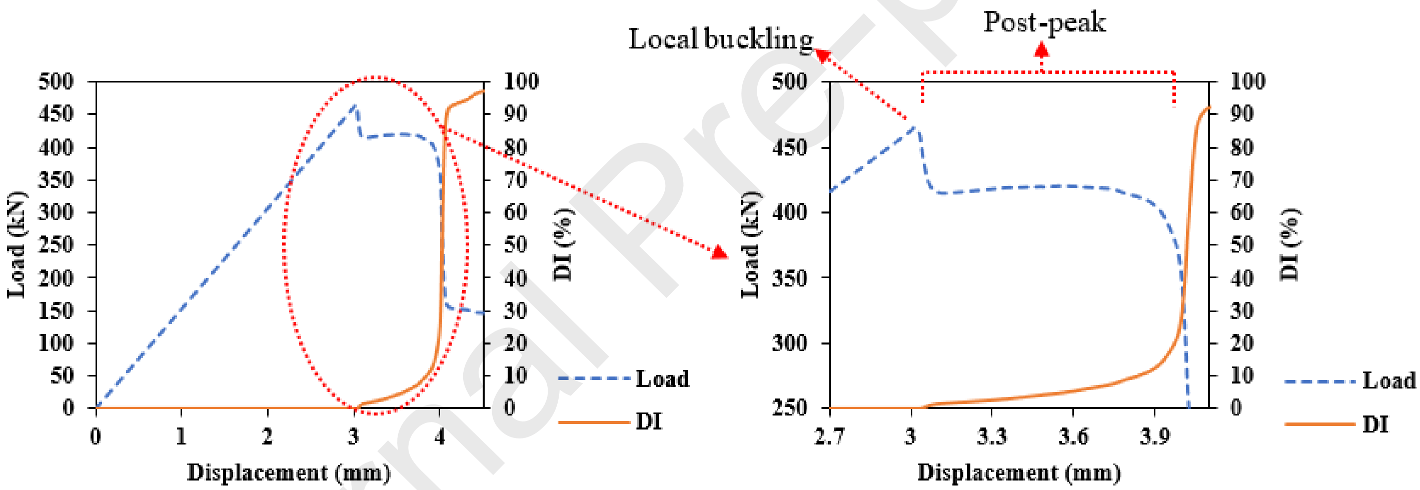

778 *Fig. 13. DI and load vs the axial displacement of S-100×100×5.2 profile with L/D equals 5.*

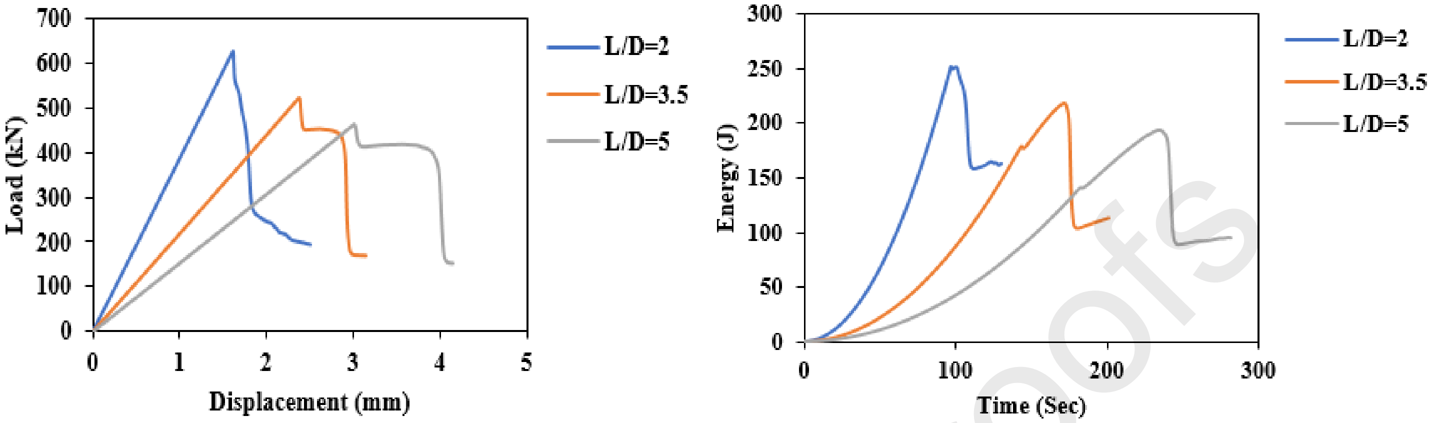

(a) (b)

Fig. 14. FEM results for S-100×100×5.2 profile with various L/D ratios (a) load-displacement curves and (b) normalised strain energy vs time.

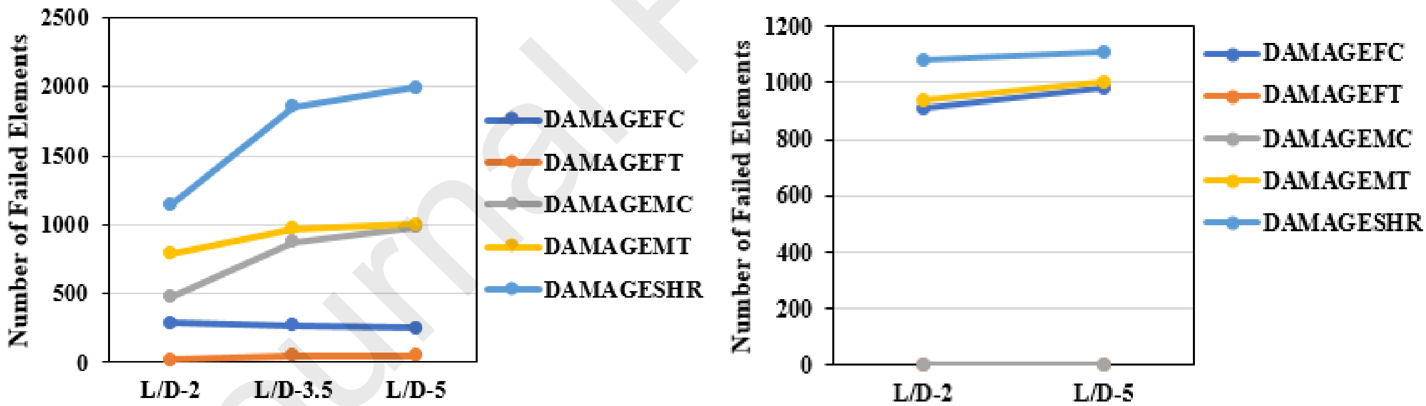

(a) (b)

Fig. 15. Density of failure modes in constituents for different L/D ratios of (a) S-100×100×5.2 profile and (b) C1-89×6.0 profile.

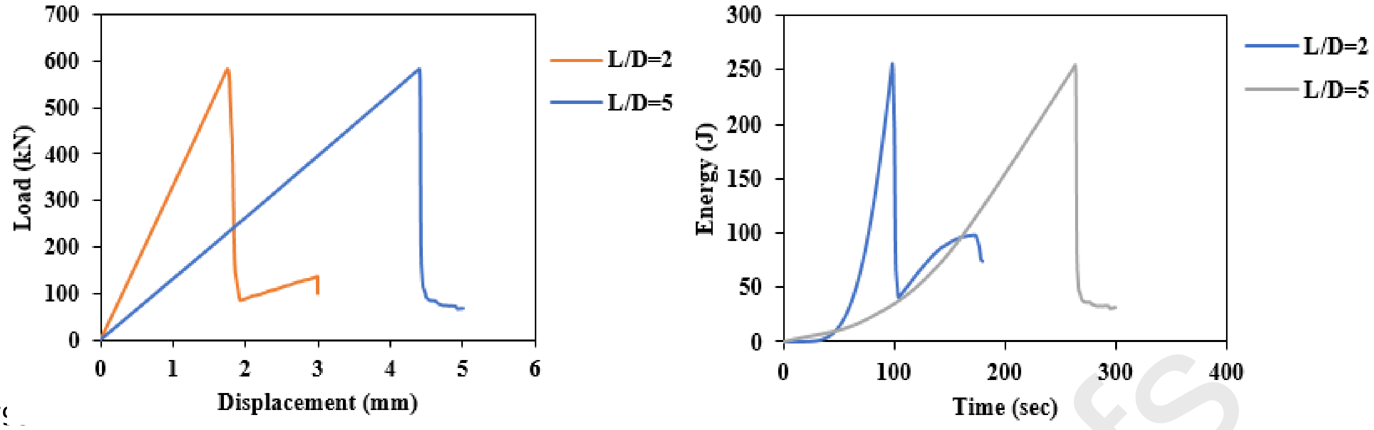

(a) (b)

Fig. 16. FEM results for C1-89×6.0 profile with various L/D ratios (a) load-displacement curves and (b) normalised strain energy vs time.

TABLES

Table 1: Geometry details of the hollow PFRP profiles.

Profile Geometry	Profile Label	Cross-sectional Area (mm^2)	Wall Thickness (mm)	L/D ratio	Length (mm)	No. specimens	
						Current study	[33]
Square	S-100×100×5.2	1910	5.2	2.0	200	5	2
				3.5	350	5	-
				5.0	500	5	2
	S-125×125×6.4	2970	6.4	2.0	250	5	-
				3.5	438	4	-
				5.0	625	5	-
Rectangular	R-75×100×5.2	1580	5.2	2.0	200	5	-
				3.5	350	4	-
				5.0	500	5	-
Circular	C1-89×6.0	1563	6.0	2.0	178	-	2
				5.0	445	-	2
	C2-89×6.0	1563	6.0	2.0	178	-	2
				5.0	445	1	2

Table 2: Composite layup properties of the hollow PFRP profiles.

Profile Label	No. of Plies	Fibre Orientation (Degree)	Fibre Content (%)
C1-89×6.0	7	[0/+56/-56/0/-56/+56/0]	0°: 74.4 56°: 25.6
C2-89×6.0	7	[0/+71/-71/0/-71/+71/0]	0°: 55.9 71°: 44.1
S-100×100×5.2	7	[0/+50/-50/0/-50/+50/0]	0°: 82.2 50°: 17.8
S-125×125×6.4	9	[0/+50/0/-50/0/-50/0/+50/0]	0°: 78.1 50°: 21.9
R-75×100×5.2	7	[0/+47.5/-47.5/0/-47.5/+47.5/0]	0°: 80.0 47.5°: 20.0

Table 3: Fibre volume fraction and lamina elastic properties of the PFRP profiles.

Profile's Label	V_f(%)	E_1 (MPa)	E_2(MPa)	v_{12}	$G_{12} = G_{13}$ (MPa)	G_{23}(MPa)
C1-89×6.0, C2-89x6.0, S-100×100×5.2, S-125×125×6.4	60.6-60.8	45700	12100	0.28	4600	4000
R-75×100×5.2	64.6	48257	12836	0.28	4861	4266

Table 4: Strength limits and fracture energy values of the pultruded lamina [34,56,57].

X^T (MPa)	X^c (MPa)	Y^T (MPa)	Y^C (MPa)	S^L (MPa)	S^T (MPa)	G_{LT} (N/mm)	G_{LC} (N/mm)	G_{TT} (N/mm)	G_{TC} (N/mm)
803	548	43	187	64	50	92	79	5	5

Table 5: Theoretical vs experimental and FEM local buckling loads of hollow box PFRP profiles.

Reference	Equation	Profile	P_{cr} [kN]	Avg. EXP Load [kN]	FEM Load [kN]
[65,66]	$N_{cr}=\frac{\pi^2}{b^2}(4.53\sqrt{D_{11}.D_{22}}+2.62(D_{12}+2D_{66}))$	S-100×100×5.2	578	589	625.1
		S-125×125×6.4	863	1002	1040
		R-75×100×5.2	497	558	591.2
[1]	$\sigma_{cr}=\frac{\pi^2}{b^2.t}(2\sqrt{5.139(D_{11}D_{22})}+2.62(D_{12}+2D_{66}))$	S-100×100×5.2	532	589	625.1
		S-125×125×6.4	801	1002	1040
		R-75×100×5.2	432	558	591.2
[6]	$N_{cr}=\frac{24}{b^2}(1.871\sqrt{D_{11}.D_{22}}+(D_{12}+2D_{66}))$	S-100×100×5.2	570	589	625.1
		S-125×125×6.4	850	1002	1040
		R-75×100×5.2	489	558	591.2
[20]	$N_{cr}=\frac{\pi^2}{b^2}(4.6\sqrt{D_{11}.D_{22}}+2.67D_{12}+5.33D_{66})$	S-100×100×5.2	588	589	625.1
		S-125×125×6.4	876	1002	1040
		R-75×100×5.2	505	558	591.2

Table 6: FEM vs experimental mechanical properties of hollow PFRP profiles.

Profile	L/D ratio	FEM modulus, E [MPa]	EXP modulus, E [MPa]	EXP SD	Error (%)	FEM strength [MPa]	EXP strength [MPa]	EXP SD	Error (%)
S-100×100×5.2	2.0	39955	40100	3217	0.36	327	308	19.5	6.16
	3.5	39904	39604	1569	0.75	274	267	5.1	2.62
	5.0	39951	41612	1334	3.99	243	252	6.7	3.57
S-125×125×6.4	2.0	38789	39100	1274	0.79	350	337	10.3	3.85
	3.5	38630	38599	1454	0.08	314	305	5.1	2.95
	5.0	38783	42301	996	8.31	277	280	8.9	1.07
R-75×100×5.2	2.0	43492	43090	2124	0.93	374	353	11	5.94
	3.5	43521	41070	1473	5.96	308	301	10	2.32
	5.0	43454	44879	2124	3.17	299	311	19.8	3.85
C1-89×6.0	2.0	37213	37100	348	0.30	373	335	53.3	11.41
	5.0	37278	37092	374	0.50	373	333	57.3	12.01
C2-89×6.0	2.0	31004	30800	237	0.66	324	308	43.5	5.19
	5.0	30979	32514	598	4.72	325	306	35.2	6.2

Mohammad Alhawamdeh: Conceptualization, Methodology, Software, Data curation, Writing- Original draft preparation. **Omar Alajarmeh, Thiru Aravinthan, Tristan Shelley, Peter Schubel, Michael Kemp, Xuesen Zeng**: Supervision, Writing- Reviewing and Editing

Declaration of interests

☒ The authors declare that they have no known competing financial interests or personal relationships that could have appeared to influence the work reported in this paper.

☐The authors declare the following financial interests/personal relationships which may be considered as potential competing interests: